Dynamical controls on the diurnal cycle of temperature in complex topography

Mimi Hughes, Alex Hall and Robert G. Fovell

Department of Atmospheric and Oceanic Sciences

University of California, Los Angeles

Los Angeles, California

corresponding author address:

Mimi Hughes

Department of Atmospheric and Oceanic Sciences

University of California, Los Angeles

Los Angeles, CA 90095

e-mail: mhughes@atmos.ucla.edu

Abstract

We examine the climatological diurnal cycle of surface air temperature in a 6-km resolution atmospheric simulation of Southern California from 1995 to the present. We find its amplitude and phase both have significant geographical structure. This is most likely due to diurnally-varying flows back and forth across the coastline and elevation isolines resulting from the large daily warming and cooling over land. Because the region's atmosphere is generally stably stratified, these flow patterns result in air of lower (higher) potential temperature being advected upslope (downslope) during daytime (nighttime). This suppresses the temperature diurnal cycle amplitude at mountaintops where diurnal flows converge (diverge) during the day (night). The nighttime land breeze also advects air of higher potential temperature downslope toward the coast. This raises minimum temperatures in land areas adjacent to the coast in a manner analogous to the daytime suppression of maximum temperature by the cool sea breeze in these same areas. Because stratification is greater in the coastal zone than in the desert interior, these thermal effects of the diurnal winds are not uniform, generating spatial structures in the phase and shape of the temperature diurnal cycle as well as its amplitude. We confirm that the simulated characteristics of the temperature diurnal cycle as well as those of the associated diurnal winds are also found in a network of 30 observation stations in the region. This gives confidence in the simulation's realism and our study's findings. Diurnal flows are probably mainly responsible for the geographical structures in the temperature diurnal cycle in other regions of significant topography and surface heterogeneity, their importance depending partly on the degree of atmospheric stratification.

1. Introduction

The simplest conception of the diurnal cycle of land surface air temperature (SAT, generally 2m temperature) is as a local energy balance between incoming surface solar radiation and net upward fluxes of sensible heat, latent heat, and longwave radiation. When the day begins, solar radiation exceeds these upward fluxes and the surface warms and stores energy. Heat storage continues and temperatures rise until the afternoon, when increasing upward fluxes become larger than declining solar radiation. When the sun goes down upward energy fluxes cool the surface and SAT drops continuously, reaching its minimum at sunrise.

In this framework, spatial variability in the SAT diurnal cycle could arise from differences in surface type. In dry regions, small latent heat fluxes would reduce the damping effect of the net upward fluxes, and SATs would be more sensitive to solar forcing than in regions where the surface is wet. In fact, moderate diurnal amplitudes are observed in high soil moisture areas such as forests, while larger amplitudes are seen in more arid regions (Aires et al., 2004; Dai et al., 2004; Jin, 2004). Spatial variability in the SAT diurnal cycle also arises from variations in reflectivity/absorptivity and effective surface heat capacity, the most prominent example of the latter being the contrast between land and water. Over the ocean, of course, the SAT diurnal cycle amplitude is virtually negligible compared to continents.

Spatial variability in the SAT diurnal cycle leads to diurnally-varying thermal gradients. These in turn generate horizontal pressure gradients and diurnal cycles in atmospheric circulation. An example of this is the classic land/sea breeze circulation,

whose phenomenology has been documented in many regions (e.g. Case et al., 2005; Atkins & Wakimoto, 1997; Simpson, 1996; Leopold, 1949). Because of the difference in SAT diurnal cycle response between dry and wet land regions, one might also expect an analogous horizontal surface flow from relatively moist to dry regions during the afternoon, with corresponding flow reversal at night. Thermally-driven diurnal flows also develop on a mountainous surface with a uniform SAT response to diurnal solar forcing simply because the surface is sloping (Rampanelli et al., 2004; Whiteman, 2000; Prandtl, 1952). This can be understood by considering a location on an idealized slope heated uniformly by the sun. The air adjacent to the slope warms significantly while the nearby free atmosphere at the same altitude does not warm as much. In a hydrostatic atmosphere this leads directly to a horizontal pressure gradient with an upslope component when projected onto the inclined surface. Thus, inclined surfaces typically experience upslope flow during daytime. Likewise, strong near-surface cooling induces downslope flow at night.

Topographically-driven diurnal winds are roughly in phase with those driven by horizontal variations in surface type because times of greatest contrast between SAT on a slope and free atmospheric temperature at the same altitude coincide approximately with times of maximum horizontal contrast in SAT response to solar forcing. In this way, diurnal winds associated with both surface type contrasts and topography can combine to form a unified diurnal circulation system (e.g. Nitis et al., 2005). The temperature contrasts driving both diurnal circulation types are in turn roughly in phase with the SAT diurnal cycle itself. Maxima in both upslope or onshore flows are observed in mid-afternoon in a region with intense topography or a coastline, while

maximum downslope or offshore flows coincide just before sunrise. Thus the simple model of the SAT diurnal cycle arising from surface energy balance considerations is the foundation for a corresponding model of bi-directional diurnal flow perpendicular to coastlines and elevation isolines, with approximately the same phasing relative to the diurnal cycle of solar radiation.

The simple energy balance model of the SAT diurnal cycle is potentially inadequate because the diurnal winds associated with it may have a component perpendicular to isentropes, and the resulting advection of potential temperature could alter the amplitude and phase of the SAT diurnal cycle. This effect is familiar to those living in coastal areas, where the sea breeze significantly moderates daytime SATs. Similarly, in a stably stratified environment, topographically-driven diurnal winds would advect lower potential temperature air upslope during the day and higher potential temperature air downslope at night, moderating the local SAT response to solar forcing. Thus, in areas with complex topography or a coastline, the basic characteristics of the SAT diurnal cycle cannot be accurately predicted without knowledge of the diurnal circulation.

The goal of this study is to examine the effect of the diurnal circulation on the SAT diurnal cycle in a coastal region with intense topography. We choose Southern California because its mountains (Fig. 1) and coastline clearly lend themselves to the development of a thermally-driven diurnal circulation system. In addition, there exist large differences in land surface properties within the region that generate large contrasts in SAT response to diurnal solar forcing, potentially also driving diurnal winds from one land surface type to another.[1] Finally, Southern California is well-suited for

[1]The variations in land surface properties can be traced to the wintertime southward migration of the mid-latitude jet stream, causing the occasional intrusion of mid-latitude disturbances into the

studying the role of stratification in determining the temperature-moderating effects of upslope and downslope flow, because its stratification varies seasonally, with the summertime atmosphere being highly stratified, while the wintertime atmosphere is only moderately so.

The very qualities that make Southern California ideal for studying this problem – its small topographic scales and diverse surface types – also make it challenging to study from a purely observational perspective. As described in section 2, the observations are suggestive of the complexity of SAT and wind diurnal cycles and links between them. However, even in this heavily-populated and relatively well-instrumented region, observations are sparse relative to the characteristic spatial scales of topography, especially at high elevations and in the desert interior (Fig. 1). To create a comprehensive picture of the diurnal cycles of SAT and wind and to study links between them a high-resolution time series with more complete spatial coverage is necessary. Thus our main conclusions are based on a 6km resolution reconstruction of regional climate generated by a regional atmospheric model downscaling known large-scale conditions from 1995 to 2003. To lend credibility to conclusions drawn from model output, a critical aspect of our study is validation of simulated SAT and wind diurnal cycles, relying on available observations and simulated data at nearest model grid points.

The paper is organized as follows: To provide background about SAT and wind diurnal cycles in the region, we present observed diurnal cycles of SAT and wind in

region. The moisture in these disturbances is mostly wrung out by the coastal mountain complexes, leaving the area between the coast and mountains moist, and the desert interior in a topographic rain shadow (Conil & Hall, 2006). During summer, the nearby North Pacific high keeps the atmosphere stable and suppresses almost all precipitation throughout the region. However, the higher soil moisture in the coastal zone lingers through to the next wet season, creating a persistent contrast in land surface properties between the coastal zone and desert interior.

section 2. The climate simulation is described and validated against observations in section 3. In section 4 we present simulated diurnal cycles of SAT and wind in detail, followed by an analysis of the effects of diurnal winds on SAT diurnal cycles in section 5. The main focus throughout sections 2-5 is on August, though this choice is arbitrary as other calendar months exhibit qualitatively similar behavior. To the extent there is seasonal variation, we demonstrate it can be interpreted in terms of the August results, so that our main conclusions apply to the entire year. In section 6 we present concluding remarks. Finally, we wish to emphasize that our focus on the climatological aspect of diurnal cycles throughout this paper implies we are only studying diurnal variability forced directly by the diurnal cycle of solar radiation, rather than synoptic atmospheric variability.

2. Observed Diurnal Cycles

a. Surface Air Temperature

Here we examine the observed SAT diurnal cycle in Southern California. To facilitate comparison with model data presented in sections 3 and 4, only stations with hourly data from 1995 to 2003 were included. For each location, an August climatological mean for each hour was created, yielding a composite SAT diurnal cycle. We eliminated stations with missing hours in the composite diurnal cycle. The resulting 30 stations are shown in Fig. 1. The observed data were provided by the California Data Exchange Center (ANZ, DEV, FMC, MLC, TAN, and VAL), the California Irrigation Management Information System (CLE, IRV, POM, SEL, and UCR), the National Climate Data Center (29P, Car, Chi, Ful, Imp, LAX, Lan, LoB, Lom, PaS, PMu, SMa,

SMo, SaB, and SaD), and the National Data Buoy Center(025, 053, and ptg). The hourly values are 8-minute averages for the NDBC data, 2-minute averages for the NCDC stations, 10-minute averages for the CDEC stations, and hourly averages for the CIMIS stations. For all four types of stations the averaging period ends on the hour.

Figure 2 shows the climatological diurnal cycle of August SAT at the 27 land stations shown in Fig. 1. (The 3 ocean stations have almost no SAT diurnal cycle.) We divided these stations into two geographical categories – desert interior and coastal – that map almost perfectly onto two types of SAT diurnal cycles. Here, a desert interior station is one separated from the ocean by mountains, with the remainder considered coastal stations, including stations within coastal mountain ranges.[2] The 6 desert interior stations (Lan, Dag, 29P, PaS, Imp, and SEL) have a diurnal cycle characterized by a daily maximum at about 4PM and almost linear rapid cooling at night. This efficient nighttime cooling is consistent with longwave radiation lost directly to space through a cloudless desert atmosphere. In contrast, the coastal stations reach their daily maximum 1-2 hrs earlier and cool slowly or almost not at all after about 9pm. This suggests the coastal stations are affected by a cooling mechanism during the day that counteracts afternoon solar heating, and a warming mechanism at night that partly counteracts radiative cooling.

b. Surface Winds

To provide a sense of how the observed diurnal winds behave, Fig. 3 shows the

[2]By our definition, some "interior" stations are actually closer to the ocean than some "coastal" stations. This is sensible because the topography precludes marine influence at the former stations, giving them a more desert-like climate.

August climatological diurnal cycle of wind at the four boxed locations in Fig. 1: Point Mugu (PMu: 34.117N, 119.117W), Anza (ANZ: 33.55N, 116.68W), Twentynine Palms (29P: 34.3N, 116.167W), and Santa Barbara (SaB: 34.43N, 119.85W); these locations were chosen as a representative sub-sample of the 30 available stations. To calculate the direction of greatest topographical gradient (black arrows, Fig. 3), we used the GLOBE 30 second topographical dataset provided by the National Geophysical Data Center's and then averaged this gradient over a 20 km by 20 km box. These diurnal wind variations are generally at least as large in magnitude as the August climatological mean winds, which were removed prior to plotting.

Point Mugu (PMu) (Fig. 3a) and Santa Barbara (SaB) (Fig. 3d) are coastal stations nearly at sea level. The diurnal winds at both locations are generally onshore during the day and offshore at night, consistent with the simple model of bi-directional diurnal flow perpendicular to coastlines and elevation isolines presented in section 1. Winds at both stations are most directly onshore around noon. The speed is greatest between 2 and 4 pm, reaching its maximum of 2.5m/s (3m/s) at Point Mugu (Santa Barbara); by this time the wind is rotated about 30° clockwise of the onshore direction. At night the wind at both stations reaches a speed of about 2.5m/s and is rotated about 30° clockwise of the offshore direction.

Anza (ANZ) lies at 1195m on the western slope of the mountain range that includes the San Jacinto Mountains. Diurnal winds here are weaker than those of Point Mugu and Santa Barbara, and reach their maximum later in the day. However, the diurnal cycle at Anza is broadly similar to the two coastal stations: Afternoon (nighttime) flows have an upslope (downslope) component, again somewhat consistent with the

simple bi-directional model. The winds also rotate clockwise. The diurnal winds at Twentynine Palms (29P), an interior station, are stronger than Anza, but are similar in that late afternoon (early morning) winds are upslope (downslope), and the winds rotate clockwise.

c. Justification for EOF analysis

The observed SAT and wind diurnal cycles presented in sections 2a and b reveal the challenge of efficiently capturing their geographical variations. Although the SAT diurnal cycle can be represented to first order by its amplitude, the observed variations in its phase and shape cannot be captured by this metric. Diurnal winds are even more challenging to characterize because they are a vector field exhibiting rotation and phase variations. These are impossible to capture by a simple metric such as the difference of the winds at two prescribed hours. We circumvent these difficulties by characterizing diurnal cycles of SAT and winds using Empirical Orthogonal Function (EOF) analysis. EOF analysis provides the spatial patterns (EOFs) and associated time series that capture the most variability within a dataset. It has been used to characterize the SAT diurnal cycle by Aires et al. (2004) and Ignatov & Gutman (1999), and to identify diurnal wind structures by Ludwig et al. (2004). It capitalizes on the fact that there is geographical coherence in the timing of diurnal cycles of SAT and wind, so that spatial structures in both SAT and wind diurnal cycles can be almost perfectly represented by just two EOFs. We refer the reader interested in learning more about the mathematical framework underpinning EOF analysis to pp. 373-398 of Wilks (1995) or Chapter 13 of von Storch & Zwiers (1999).

All EOFs in this paper are computed from the covariance matrix of the compos-

ite diurnal cycle with the monthly mean removed. For the wind data, we computed joint EOFs of the meridional and zonal components to maximize their joint variance (Wilks, 1995, pp. 390). We also use EOF analysis to compare modeled and observed diurnal cycles. As we will demonstrate, this method allows us to validate amplitude and phase/shape variations of the SAT diurnal cycle separately. In addition, we can validate the non-scalar diurnal winds without a detailed and cumbersome comparison of complex wind roses.

d. Observed modes of variability

The right column of Fig. 4 shows EOF analysis of the SAT composite diurnal cycle at the 30 stations. The first two EOFs (EOF1 and EOF2) capture nearly 100% of the variance, so that for each station, the SAT diurnal cycle can be nearly perfectly reconstructed as a linear combination of these two EOFs, with weights over the course of the day determined by their associated time series. The time series associated with SAT EOF1 (Fig. 4f) closely resembles a classic SAT diurnal cycle governed by the simple energy balance model presented in section 1: temperature increases from sunrise until about 3pm, when it begins to decrease, reaching its minimum around sunrise.

The loading magnitudes of SAT EOF1 (Fig. 4b) vary from about 0 K to 7 K, whereas the loading magnitudes of SAT EOF2 (Fig. 4d) only vary from -1.5 K to 1.5 K. Because of its large magnitude relative to SAT EOF2, the SAT diurnal cycle shape at any given location closely resembles the time series associated with SAT EOF1, and SAT EOF1's loading magnitude corresponds to diurnal cycle amplitude. This interpretation is confirmed by the nearly perfect inter-station correlation between the SAT EOF1 spatial loadings and SAT diurnal cycle amplitude (correlation coefficient=0.99). The

time series associated with SAT EOF2 is approximately in quadrature with the SAT EOF1 time series, and the small SAT EOF2 loading magnitudes are manifestations of noteworthy variations in the shape and phase of the SAT diurnal cycle discussed in section 2a: Five of the six inland stations (black lines, Fig. 2), with strong nocturnal cooling and late afternoon SAT maxima, have negative values for SAT EOF2. The other 21 stations, with curiously small nocturnal cooling (gray lines, Fig. 2) and early afternoon SAT maxima, have positive or very small values for SAT EOF2.

When EOF analysis is performed on the composite wind diurnal cycles with the mean winds removed at the 30 stations of Fig. 1, the result is also two EOFs accounting for almost all variance (Fig. 4, left column). As with SAT, the two EOFs can be combined with their associated time series to reconstruct the diurnal winds. Here we briefly illustrate this, using diurnal winds at Anza and Santa Barbara shown in Fig. 3 as examples.

At Anza, the two EOFs are similar in magnitude, and wind EOF2 is rotated about 60° counterclockwise from wind EOF1. Comparing the direction of EOF1 (Fig. 4a) with the direction of the elevation gradient at Anza (Fig. 3b), we see that EOF1 corresponds roughly to variations in upslope and downslope flow. According to its associated time series (Fig. 4e, dashed light blue line), it reaches its maximum upslope value at about 4pm. Wind EOF2 (Fig. 4c) represents variations in the flow in the direction approximately parallel to contours of constant elevation. It reaches its largest magnitude a few hours before wind EOF1 (Fig. 4e, dashed light red line). Combining the two EOFs results in a wind rotated counterclockwise from upslope in the early afternoon, nearly upslope in mid-afternoon, and slightly clockwise of upslope in the late afternoon (i.e.

the violet, maroon, and red arrows on Fig. 3b, respectively). Thus the 2nd EOF is required to capture the observed clockwise rotation in Anza's diurnal winds.

Santa Barbara has large loading in both EOF1 and EOF2, but unlike Anza, the two wind EOFS are nearly parallel to one another, both being oriented approximately in the onshore direction. This implies the flow is predominantly onshore or offshore at all times, but that the strength of the flow is not in phase with EOF1. The time series associated with EOF1 reaches its minimum at 7AM, implying maximum flow in the offshore direction at that time. Yet according to Fig. 3d, the maximum offshore winds at Santa Barbara occur around midnight. By incorporating the contribution of EOF2, which corresponds to maximum offshore flow at 10 pm, the observed phasing of the offshore flow is obtained.

These two examples make it clear that wind EOF1 corresponds mostly to flow across the coastline and elevation isolines. Because the time series associated with wind EOF1 (Fig. 4e, light blue) is well-correlated to that of the main mode of SAT diurnal variation (SAT EOF1, Fig. 4e, dark blue), we interpret wind EOF1 as representing our simple bi-directional model of wind response to solar-forced diurnal warming and cooling. Meanwhile, wind EOF2 represents departures from this simple model, just as SAT EOF2 represents departures from from the expected SAT diurnal cycle. At locations where wind EOF2 makes a significant angle to wind EOF1, it captures diurnal wind rotation. When EOF2 is parallel to EOF1, it oscillates in a bi-directional fashion as expected from the simple model, but is out of phase with the expected thermal forcing.

3. Southern California climate simulation

The information presented in section 2 hints at the complexity of SAT and wind diurnal cycles in Southern California and the potential influence of the winds on SAT. However, because observations are so sparse relative to the characteristic spatial scales of the topography (see Fig. 1), we cannot determine how representative the observations are of the diurnal cycles in the region's unsampled areas. In addition, the observational data contain only a few surface variables, preventing us from rigorously investigating mechanisms involved in generating the diurnal cycles. Reanalysis products offer a full suite of 3-D variables, but still are likely too coarse in resolution; for example, the North American Regional Reanalysis (Mesinger et al., 2006), with a 32 km grid spacing, resolves only the grossest terrain features in Southern California, and therefore probably does not adequately resolve spatial variations in the diurnal cycles. Here we circumvent the resolution problem by relying on a multi-year 6-km resolution simulation of the southern third of California.

a. Configuration

This simulation was created with the Penn State/NCAR mesoscale model version 5, release 3.6.0 (MM5, Grell et al., 1994). The 6 km domain was nested within an 18 km domain covering southern California and parts of Arizona, Nevada, and Mexico, which was likewise nested within a 54 km domain encompassing most of the western US (Fig. 5). Comparing the terrain of the 6 km domain (Fig. 6) with Fig. 1, we see that at this resolution, all major mountain complexes in Southern California were represented, as were the Channel Islands just off the coast. The dimensions of each domain were 35x36, 37x52, and 55x97 for the 54, 18, and 6 km domains, respectively, and the nesting was two-way for both interior domains. Each domain had 23 vertical levels, with the

vertical grid stretched to place the highest resolution in the lower troposphere. In the outer two domains, the Kain-Fritsch 2 (Kain, 2002) cumulus parameterization scheme was used. In the 6km domain, only explicitly resolved convection could occur. In all domains, we used the MRF boundary layer scheme (Hong & Pan, 1996), Dudhia simple ice microphysics (Dudhia, 1989), and a radiation scheme simulating longwave and shortwave interactions with clear-air and cloud (Dudhia, 1989).

The terrain used in the simulation was generated from the United States Geological Survey (USGS) 30-second global elevation data, GTOPO30. [3] Additionally, each gridpoint was assigned a land surface type (corresponding to the dominant vegetation within the gridbox) based on the 25 category 30-second USGS version 2 land cover data. This index then points to a look-up table which contains summer (15 April-15 October) and winter (15 October- 15 April) values for albedo, available moisture, emissivity, roughness length, and thermal inertia.

The boundary conditions came from the National Center for Environmental Prediction's 40-km resolution Eta model analysis data from the National Center for Atmospheric Research's archive. The time period covered was from May 1995 to December 2003. Throughout this period, MM5 was initialized every 3 days at 18Z (10am local time) and run for 78 hours, with the first six hours being discarded as model spin-up. The interior boundary conditions and sea-surface temperatures were updated at each initialization, with the lateral boundary conditions updated continuously throughout the run. Thus the simulation in the 6-km nest acts as a reconstruction of the local atmospheric conditions based on known large scale atmospheric conditions. Correlat-

[3]This is different from the data used to generate Figure 1.

ing this simulation's daily-mean winds with available observations, Conil & Hall (2006) verified that the simulation captures synoptic time-scale variability in the daily-mean wind, confirming the effectiveness of this downscaling technique in reconstructing local circulation anomalies.

b. Validation

In the previous section, we determined that observed diurnal cycles of SAT and wind can be characterized by two modes of variability capturing nearly all of the variance. Here we verify that EOF analysis of simulated August composite diurnal cycles of SAT and wind sub-sampled at the 30 gridpoints closest to the observation stations gives similar results. Differences between simulation and observation may arise from errors in both, or from topographic differences between the two datasets. Simulation errors could stem from biases in initial or boundary conditions, incorrect model physics, from fine-scale structures in SAT or wind unresolved at 6km, or from processes absent from the simulation such as topographic shading (Colette et al., 2003). Observed SATs and winds also certainly contain systematic and random measurement error, with the effects of random measurement error being exacerbated when sample sizes are small. Obvious cases of this are noted in the caption of Fig. 2.

Despite these error sources, EOF analysis of simulated SATs sub-sampled at the 30 closest gridpoints (Fig. 7d, only time series is shown) gives similar results to observations: two EOFs account for nearly all variance, with the first accounting for 97%, and the second accounting for 2%. The time series associated with the model SAT EOFs also agree very well with their observed counterparts. Meanwhile, the spatial correlation between the loading magnitudes of modeled and observed EOFs is 0.83 for

EOF1 and 0.59 for EOF2, indicating the model captures spatial variations of both EOFs reasonably well.

EOF analysis of the diurnal winds also produces very similar results for the simulation and observations (Fig. 7, a-c). Analysis of sub-sampled MM5 winds results in two EOFs accounting for nearly all of the variance, and the two EOFs also account for similar proportions of the variance as the observations (71% and 24%). EOF1 of the model winds agrees broadly with its observed counterpart: First, the time series associated with simulated and observed wind EOF1 are quite similar (Fig. 7c, blue lines). The amplitudes and directions of model and observed EOF1 loadings are also very similar (Fig. 7a). The agreement in orientation of simulated and observed wind EOF1 loadings and the nearly perfect correlation (correlation coefficient = 0.93) of the time series associated with simulated and observed EOF1 indicates that like its observed counterpart, simulated wind EOF1 corresponds to a bi-directional flow oscillation perpendicular to the coastlines and elevations isolines in phase with the SAT diurnal cycle. Differences between model (Fig. 6) and actual topography (Fig. 1) will result in differences in the direction of the local elevation gradient, and may explain disagreements between model and observations in the direction of EOF1. For example, at Anza (Fig. 7a) the model topography gradient is rotated 26° counter-clockwise from the actual terrain gradient, resulting in the simulated diurnal winds at Anza being similarly rotated. However, these differences are generally slight, suggesting topographic features responsible for generating this component of the wind diurnal cycle are resolved with 6km grid spacing.

The time series associated with simulated wind EOF2 is also very similar to its

observed counterpart (Fig. 7c, red lines), so that model wind EOF2 can also be interpreted as representing either rotation or phase departures from the simple bi-directional model. Most inland locations have excellent agreement in magnitude and direction between model and observed EOF2 loadings (e.g. Twentynine Palms). Meanwhile at most coastal locations, simulated and observed EOF2 loadings are both small (not shown here for the model, though visible for the observations in Fig. 4c). This, together with the agreement in EOF1 noted above, indicates simulated diurnal winds at these locations have the correct amplitude, sense of rotation, and phase. At Anza simulated EOF2 disagrees with observed EOF2, as was the case with EOF1. However, the *angle* between EOF1 and EOF2 is about the same for the simulation and observations. This indicates that the phase and sense of rotation is in agreement at Anza, but that the major axis along which the winds blow differs, which is entirely accounted for by inadequately-resolved topography in the model. In a few coastal locations, there are differences in EOF2 that are more difficult to account for: For example, at Point Mugu and Santa Barbara, the direction of EOF2 with respect to EOF1 indicates that EOF2 introduces a strong rotational component into the model winds, while EOF2 instead introduces a phase difference into the observed winds.

In summary, the sub-sampled model SAT and wind agree reasonably well with observations throughout the domain: Both observations and model have two dominant modes of variability in SAT and wind, which each represent approximately the same proportions of variance. The associated time series are in very good agreement between model and observations, and the spatial patterns of the EOFs are in reasonable agreement. The fact that the model is satisfactorily capturing the observed diurnal cycles at

all 30 locations well is further confirmed by the root mean square error of the diurnal cycles with monthly mean removed, which is on average 1.5 K for SAT, 0.93m/s for wind speed, and 65° for wind direction. It is possible the agreement is fortuitous because it results from the observations being located in areas where the simulation's fidelity is particularly high. However, this is highly unlikely, since the observation stations are reasonably well-distributed throughout the model domain.

4. Modes of simulated variability

Having confirmed the simulation captures observed diurnal variation of SAT and wind reasonably well, we take advantage of its full spatial coverage and high resolution to develop a comprehensive picture of the diurnal cycles of SAT and wind. We first show results for August, then illustrate that the results are applicable year-round (section 4b).

a. August

EOF analysis on the August composite SAT diurnal cycle is shown in Fig. 8. Once again the first two EOFs capture nearly all variance, and their relative importance is similar to observations and the sub-sampled SAT field. Their associated time series are nearly identical to those of the sub-sampled model SATs (Fig. 8c), indicating the modes of the sub-sampled model SATs are expressions of the true simulated modes of diurnal variability at the sampled locations. This further suggests the observed modes, despite being handicapped by sparse sampling, are likely to be representative of the actual modes of diurnal variability at the observation locations.

As with observations, the simulated loading magnitudes of EOF1 (Fig. 8a) represent SAT diurnal cycle amplitude. This is confirmed by the nearly perfect spatial correlation

between EOF1 loadings and simulated SAT diurnal amplitude (0.996). The full model field provides a comprehensive picture of the SAT diurnal cycle amplitude impossible to obtain from observations. For example, EOF1 loading magnitudes are curiously low in high elevation areas, a pattern completely missed in the observation SAT EOF1 (Fig. 4b). In addition to decreasing with elevation, EOF1 loadings generally increase with distance from the coast, so that low-lying desert interior regions have the largest SAT diurnal amplitude, while high-elevation and coastal regions have the smallest.

Simulated SAT EOF2, like its observed counterpart, represents variations in the shape and phase of the SAT diurnal cycle. In regions where EOF2 loadings are negative, such as the San Joaquin Valley (35N, 119W) and Mojave Desert, the SAT diurnal cycle is characterized by a late afternoon maximum and strong cooling at night. At high elevations and near the coast where EOF2 loadings are positive, SAT reaches its reaches its maximum earlier in the day, reaches its minimum in late evening, and then remains steady through the night. This interpretation of EOF2 is confirmed by Fig. 9, which shows two composite SAT diurnal cycles of locations segregated by positive and negative extremes in EOF2. In the observational data, we saw these two differently-shaped diurnal cycles when the stations were segregated by location (Fig. 2). Here we confirm that when the SAT diurnal cycle throughout the region is considered, this geographical separation is roughly equivalent to segregating by EOF2 loading values, since negative EOF2 loadings correspond to points in the desert interior, while positive loadings correspond to locations in the coastal zone.

Figure 10 shows the EOFs for the full simulated wind field for August. Once again the first two EOFs capture nearly all variance, and their relative importance is similar

to observations and the sub-sampled model wind field. Their associated time series are also nearly identical to those of the sub-sampled model winds (Fig. 10c). Fig. 10a shows the spatial variation in the magnitude and direction of EOF1 loadings, the flow in phase with SAT EOF1. In general, the dominant mode of the SAT diurnal cycle is directly associated with flow across the coastline and elevation isolines, resulting in strong convergence (divergence) during the day (night) at mountain tops. There is a general correspondence between speeds of these flows and either the magnitude of the elevation gradients or the presence of coastline. These facts conform to our simple model of wind response to thermal forcing. The spatial extent of the land/sea breeze over the ocean is also apparent from EOF1: It falls off rapidly beginning about 20 km from the shore, and is negligible about 120 km from shore. Ding et al. (2004) found a similar penetration scale for the land/sea breeze in Southeast Asia.

EOF1 of the full model wind field also reveals that in the interior large scale thermal gradients associated with horizontal contrasts in land surface type can overwhelm topographically-driven diurnal flows. For example, in the two passes on the east and west flanks of the San Gabriel Mtns (34.3N, 117.8W), EOF1 magnitude is large and directed toward the desert interior, even though this implies downslope (upslope) flow during the day (night) on the desert side of the passes. Winds are similarly downslope (upslope) during the day (night) in the mid-eastern part of the domain (115.5W to 116.5W, 33.5N to 34N) on the northern slopes of the Little San Bernardino Mtns just northwest of the Salton Sea. These winds are likely the signature of a larger scale circulation toward the Mojave Desert during the day and out of the desert at night, driven by large thermal response of the desert surface to the solar diurnal cycle. Ohashi

and Kida (2002) and Stewart et. al. (2002) also found evidence of competition between topographically-forced diurnal winds and diurnal winds forced by large-scale horizontal contrasts in surface type in Southern Japan and Utah, respectively.

The magnitude of simulated wind EOF1 is generally larger than that of EOF2 (Fig. 10b) throughout the domain, implying the maximum diurnal wind speeds mostly coincide with the pre-dawn and mid-afternoon extrema of the time series associated with EOF1 (Fig. 10c). However, in some parts of the domain, where observations happen to be largely absent, such as in the Mojave Desert (116.5W to 118W, 34.5N to 35.5N) and on the eastern slopes of the north-south oriented mountain complex west of the Salton Sea (116.5W, 32.5N to 34N), EOF2 is large in magnitude relative to EOF1. This implies the wind speeds in those regions reach their maxima when extrema occur in the time series associated with EOF2. In these regions, a peak in wind speed occurs around 10AM, and represents upslope flow, while another peak corresponding to downslope flow occurs around 9PM. Similar to observations, winds in coastal areas have a particularly small EOF2 component, indicating the diurnal flow is dominated by a simple land-sea breeze in phase with the SAT diurnal cycle. An exception is seen over the ocean extending from Santa Barbara and throughout the Channel Islands area, where the two EOFs are about equal and at right angles to one another. This indicates simulated diurnal winds there exhibit clockwise rotation, with onshore (offshore) flow during the afternoon (late night), and alongshore flows in early evening and mid-morning. The clockwise rotation of the sea breeze along the coast near Santa Barbara may reflect the influence of the Coriolis force (e.g. Rotunno, 1983; Haurwitz, 1947), though there is some debate about the role of the Coriolis force in the sea breeze (Simpson, 1996).

To emphasize the climatological importance of these diurnal winds, Table 1 (top two rows) shows the magnitudes of the diurnal winds and the monthly mean August wind, where the diurnal winds are represented by the total length of the wind vector along its major (EOF1) and minor (EOF2) axis of rotation. Although over the ocean the monthly mean wind dominates, over land the average diurnal wind is about 60% (40%) percent larger than the mean along its major (minor) axis. Thus over land the diurnal winds are the dominant feature of the region's climatological circulation.

b. Annual variation

The patterns of Figs. 8 and 10 are representative of SAT and wind diurnal cycles not only for August, but for every month of the calendar year. To demonstrate this, we performed EOF analysis on simulated SAT and wind composite diurnal cycles for every month individually. In every case there are two EOFs explaining nearly all variance (SAT: not shown, wind: Fig. 12c). The shape and phasing of the time series associated with EOF1 for each month (not shown) is very similar to that associated with August EOF1 for both SAT and wind. The main seasonal variation is that in the winter months, the time spent going from minimum to maximum of EOF1 shortens and the time spent going from maximum to minimum lengthens, corresponding to a shorter day and longer night. This confirms that EOF1 represents the diurnal SAT and wind variations directly linked to the solar forcing throughout the year. The timing and shape of EOF2 also changes very little with calendar month for both SAT and wind, so that throughout the year EOF2 represents shape and phase deviations in the case of SAT, and rotation and phase deviations in the case of winds.

To emphasize this year-round persistence, we show the two dominant SAT and wind

EOF loadings from February (Figs. 11 and 12), the opposite phase of the annual cycle from August. SAT EOF1 for February (Figs. 11a) has a very similar pattern to August. Differences between the two months can be explained by the much larger August solar forcing. For example, the loading magnitudes of SAT EOF1 are generally about one and one-half times as large in August. Further, the seasonal contrast in SAT EOF1 loadings is largest in very arid regions and smallest near the coast and at high elevations. This is consistent with much higher sensitivity of the desert to elevated solar forcing in August relative to the moister coastal zone. The spatial pattern of February's SAT EOF2 loadings (Figs. 11b) is also very similar to August's, although again their magnitudes are about half as large, indicating that shape and phase differences between the coastal zone and desert interior are reduced in winter.

Comparing Figs. 10a and 12a we see that in both months the wind EOF1 loadings consist primarily of flow perpendicular to the coastline and elevation isolines, though in February EOF1's loading magnitudes are smaller, consistent with reduced wintertime solar forcing. Furthermore, in August the diurnal cycle of circulation into and out of the desert (Fig. 10a) is about twice as strong as the land/sea breeze, while in February (Fig. 12a) the flow into the desert is the same magnitude as the land/sea breeze. This results from the desert's higher sensitivity to August's increased solar forcing (evident in Fig. 11a). The features of February's EOF2 (Fig. 12b) are also broadly similar to August's (Fig. 10b). The maximum values of EOF2 loadings for both months are on the eastern slopes of the north-south oriented mountain complex west of the Salton Sea (116.5W, 32.5N to 34N) and over the ocean south of Santa Barbara. Finally, like August, the diurnal winds in February over land are large compared to the monthly

mean winds (table 1, bottom two rows).

5. Dynamical Impact on Surface Air Temperature Diurnal Cycles

The timing of the two EOFs for SAT and wind (Fig. 13) is virtually identical, suggesting mechanistic links between diurnal variability of SAT and wind. Here we present a possible mechanism to explain the departures of the diurnal cycle from the simple models presented in section 1; proving with certainty this mechanism is dominant in determining the SAT diurnal cycle in Southern California would require detailed analysis of the thermodynamic budget, which is beyond the scope of this paper. However, given the high degree of consistency of our arguments with the patterns we show, this mechanism very likely plays the dominant role in determining the diurnal cycle in coastal Southern California.

We have already seen that in the case of both variables, the phasing of EOF1 implies a correspondence with the simple models of SAT and wind diurnal cycles presented in section 1. However, the flows represented by wind EOF1 also affect SAT, creating a feedback that modifies the spatial structure of SAT EOF1 (Fig. 8a). This advection effect is familiar in the moderating influence of the daytime sea breeze as cool ocean air is advected over warm land. The signature of this suppression of daily maximum SATs is seen in reduced SAT diurnal cycle amplitudes (SAT EOF1) in the coastal zone, especially within 30 km of the coast. An analogous advection effect takes place in conjunction with the diurnal flows across elevation isolines, and arises from the fact that the lower troposphere is generally stably stratified throughout Southern California,

especially during August (Fig. 14a). During the daytime, air of cooler potential temperature from lower elevations converges at mountaintops, suppressing daily maximum SATs there, while nighttime divergence at mountaintops draws down higher potential temperature air from above, raising minimum SATs at night. This explains why the magnitude of SAT EOF1 is so curiously small at mountaintops. Downslope flow at night also raises minimum SATs in the coastal zone, further reducing SAT diurnal cycle amplitudes there. The advection effect is strongest where diurnal flows have a component perpendicular to densely-packed isentropes, such as at the coastline, and where diurnal flows perpendicular to isentropes reinforce one another through convergence or divergence, such as at mountaintops.

The advective cooling effect of daytime onshore and upslope flows tips the balance between solar heating and cooling influences toward cooling earlier in the day, advancing the daily maximum of SAT. Similarly, advective warming effects of downslope and offshore flows counteract radiative cooling at night, so that SATs drop little, if at all. Thus the advection effects of wind EOF1 not only generate spatial variations in SAT diurnal cycle amplitude but also spatial variations in the shape and phase of the SAT diurnal cycle, represented by SAT EOF2 (Fig. 8b). This is corroborated by a rough inverse relationship in geographical variations of SAT EOF1 and SAT EOF2, particularly in the coastal zone: at mountaintops and near the coast, where advection effects most strongly suppress SAT diurnal cycle amplitude (small SAT EOF1), SAT also peaks earlier in the daytime and falls little at night (positive SAT EOF2).

In contrast to the coastal zone, SAT EOF2 values in the desert interior are consistently negative. This is likely because the atmosphere is considerably less stable there

(Fig. 14a), so that the advection effect associated with wind EOF1 is much weaker. A rough balance between incoming solar radiation and upward surface energy fluxes prevails, and SAT peaks later in the afternoon and drops consistently throughout the night.

This contrast between the coastal zone and desert interior is illustrated for the nighttime case in Fig. 14b, which shows the nighttime average of a longitude-height cross-section of simulated climatological August potential temperature across the southern part of the domain. The transect was chosen to slice across the interior and coastal zones. (See line AB in Fig. 14a.) It clearly shows the coastal zone air is much more stably stratified than the desert interior air throughout the night. Advection and radiative cooling, two major components of the nighttime thermodynamic budget, are illustrated in Fig. 14b: nighttime winds perpendicular to the mountain range are shown by red arrows, and radiative cooling is indicated schematically with black arrows. Because of greater stratification, advective warming is larger at the mountaintop and on the coastal side of the mountain than on the interior side of the mountain. Conversely, SAT is much higher at interior locations, causing the radiative cooling to be greater. The resulting combination between advection and radiative cooling causes SAT to decrease dramatically at night in the interior and remain constant at the mountaintop and on the coastal side of the mountains.

A visual comparison of the second EOFs of SAT and winds (Figs. 10a and 8a) over land reveals a relationship between wind EOF2 and the phase variations in SAT represented by SAT EOF2. This likely occurs because the gradients of SAT EOF2 have a corresponding signature in the pressure gradient field, which in turn drive a circula-

tion similar to wind EOF2. To quantify the relationship between wind EOF2 and the gradient of SAT EOF2, we calculated the spatial correlation of the divergence of these two quantities and found they are reasonably well-correlated (correlation coefficient = 0.54). We further illustrate this physically intuitive result by considering the region west of the Salton Sea, which has the largest values for wind EOF2. SAT EOF2 on the mountains in that region is positive and relatively large, meaning that at night SATs do not decrease after about 9 pm. By morning the air is much warmer than the air just to the east, which has cooled vigorously all night (negative SAT EOF2). This thermal dipole causes a pressure gradient from west to east, and the winds respond by blowing from east to west early in the morning, precisely the pattern of wind EOF2. This tight correspondence between EOF2 of SAT and wind indicates that the cause of the departures of the winds from the simple bi-directional model are distortions of the SAT diurnal cycle.

6. Summary and Implications

The climatological diurnal cycles of SAT and winds in the southern third of California are investigated using both a network of 30 observation stations and a 6-km mesoscale model simulation. The simulation was created using the MM5 model to dynamically downscale the Eta reanalysis from 1995-2003. The simulation can be thought of as a reconstruction of the local weather and climate, constrained by MM5 physics, the 6-km resolved surface conditions, and the known large-scale atmospheric conditions. We verified that the simulated SAT and wind diurnal cycles are similar to those at the 30 observation stations, then used the simulation to examine dynamical controls of SAT

diurnal cycles.

To simplify and streamline the analysis of SAT and wind diurnal cycles, we applied EOF analysis to the climatological August diurnal cycles of SAT and wind. For both SAT and wind the first two EOFs capture nearly all diurnal variance, with EOF1 primarily representing what we would expect from a simple model of the diurnal cycle: SAT reaches its maximum 2-4 hours after the noontime maximum in solar heating, and reaches its minimum at sunrise, with spatial gradients caused only by differential partitioning in sensible and latent heating, as well as surface differences in heat capacity. This large daily warming and cooling over land induces the land/sea breeze, as well as flows across elevation isolines which cause convergence (divergence) at mountaintops during the day (night). Additionally, large scale thermal gradients associated with contrasts in land surface type between the desert interior and the coastal regions induce a circulation into/out of the desert, which can overwhelm the local upslope/downslope tendency. Over land, these thermally driven diurnal winds have nearly double the magnitude of the monthly average winds, and so are the dominant feature of the region's climatological circulation.

Throughout the region, the diurnal winds of EOF1 have a component perpendicular to isentropes, affecting the amplitude of the SAT diurnal cycle. As expected, the daytime sea breeze reduces daily maximum temperatures in the land area adjacent to the coast. Southern California's atmosphere is stably stratified, so that diurnal flows across elevation isolines also have a component perpendicular to isentropes. Therefore the nighttime land breeze advects air of warmer potential temperature downslope toward the coast, raising minimum temperatures in land areas adjacent to the coast.

Further inland, upslope (downslope) flows also advect air of cooler (warmer) potential temperature to higher (lower) elevations during daytime (nighttime). This moderates SAT maxima (minima) where upslope (downslope) flows converge (diverge) at mountaintops. The quantitative impact of this mechanism depends on the overall balance of the thermodynamic budget, which is beyond the scope of this paper.

By advecting potential temperature, diurnal winds also affect SAT phase and shape (SAT EOF2). During the day the large advective cooling in the coastal zone not only reduces SAT maxima, but also causes it to occur approximately two hours earlier than in the interior. Further, because vertical stratification is greater in the coastal zone than in the desert interior, the winds introduce significant spatial structure into the shape of SAT's diurnal cycle. In the coastal zone over land, the nighttime advective warming is large enough to counter the effects of radiative cooling, so that temperatures reach their minimum well before sunrise and thereafter remain steady. In the interior, by contrast, advective warming is smaller than radiative cooling, leading to a continuous nighttime drop in temperature. This is in agreement with the large differences between the interior observed SAT diurnal cycles, characterized by dramatic nighttime cooling, and those within the coastal zone, which reach minimum values around 9pm and remain steady through the night. The geographical variations in the shape and phase of the SAT diurnal cycle–ultimately caused by variations in vertical stratification–also induce corresponding pressure gradients. These in turn drive secondary diurnal wind anomalies, which manifest themselves either as rotation in diurnal wind direction or deviations in the timing of maximum flow (wind EOF2). This mechanism probably also accounts for the curious rotation and phase variations of the observed diurnal winds

seen in section 2b.

Our study shows that in a region of complex topography, mesoscale climate dynamics govern the temporal and spatial structures of diurnal cycles of SAT. These dynamics should apply to other regions, subject to two caveats. First, as seen in section 4b where we examined the annual variation in these dynamics in Southern California, the diurnal winds' impact on SAT depends on the strength of vertical stratification. Therefore, in the many regions less stably stratified than Southern California, we expect dynamical links between winds and SAT to be consistently weaker. Second, by focusing on the dry summer climate in Southern California, we've been able to isolate the influence of these winds without the additional complexity of the interaction between diurnal SAT, winds, and cloudiness: In moister regions, we expect enhancement of mountaintop cloud fields in the afternoon, with reduced solar radiation leading to additional suppression of daytime maximum temperatures, and hence diurnal cycle amplitude. These additional complexities could also impact the rotation of the climatological diurnal winds.

Acknowledgments. Mimi Hughes is supported by an NSF gradaute student fellowship and NSF ATM-0135136, which also supports Alex Hall. Robert Fovell is supported by NSF ATM-0139284. Opinions, findings, conclusions, or recommendations expressed here are those of the authors and do not necessarily reflect NSF views.

References

Aires F, Prigent C, Rossow WB (2004) Temporal interpolation of global surface skin temperature diurnal cycle over land under clear and cloudy conditions. J. Geophys. Res. 109:doi:10.1029/2003JD003527.

Atkins NT, Wakimoto RM (1997) Influence of the synoptic-scale flow on sea breezes observed during CaPE. Mon. Wea. Rev. 125:2112–2130.

Case JL, Wheeler MM, Manobianco J, Weems JW, Roeder WP (2005) A 7-yr climatological study of land breezes over the Florida spaceport. J. Appl. Meteor. 44:340–356.

Colette A, Chow FK, Street RL (2003) A numerical study of inversion-layer breakup and the effects of topographic shading in idealized valleys. J. Appl. Meteor. 42:1255–1272.

Conil S, Hall A (2006) Local regimes of atmospheric variability: a case study of Southern California. J. Climate 19:4308–4325.

Dai A, Trenberth KE, Karl TR (2004) Effects of clouds, soil moisture, precipitation, and water vapor on diurnal temperature range. J. Climate 12:2451–2473.

Ding A, Wang T, Zhao M, Wang T, Zongkai L (2004) Simulation of sea-land breezes and a discussion of their implications on the transport of air pollution during a multi-day ozone episode in the Pearl River Delta of China. Atmos. Env. 38:6737–6750.

Dudhia J (1989) Numerical study of convection observed during the winter monsoon experiment using a mesoscale two-dimensional model. J. Atmos. Sci. 46:3077–3107.

Grell GA, Dudhia J, Stauffer DR (1994) A description of the fifth-generation Penn State/NCAR Mesoscale Model (MM5). Technical report NCAR Tech. Note NCAR/TN-398+STR.

Haurwitz B (1947) Comments on the sea-breeze circulation. J. Meteor. 4:1–8.

Hong SY, Pan HL (1996) Nonlocal boundary layer vertical diffusion in a Medium-Range Forecast Model. Mon. Wea. Rev. 124:2322–2339.

Ignatov A, Gutman G (1999) Monthly mean diurnal cycles in surface temperatures over land for global climate studies. J. Climate 12:1900–1910.

Jin M (2004) Analysis of land skin temperature using AVHRR observations. Bull. Amer. Meteor. Soc. 85:587–600.

Kain JS (2002) The Kain-Fritsch convective parameterization: An update. J. Appl. Meteor. 43:170–181.

Leopold LB (1949) The interaction of trade wind and sea breeze, Hawaii. J. Atmos. Sci. 6:312–320.

Ludwig FL, Horel J, Whiteman CD (2004) Using EOF analysis to identify important surface wind patterns in mountain valleys. J. Appl. Meteor. 43:969–983.

Mesinger F, DiMego G, Kalnay E, Mitchell K, Shafran P, Ebisuzaki W, Jovi D, Woollen J, Rogers E, Berbery EH, Ek MB, Fan Y, Grumbine R, Higgins W, Li H, Lin Y, Manikin G, Parrish D, Shi W (2006) North American Regional Reanalysis. Bull. Amer. Meteor. Soc. 87:343–360.

Nitis T, Kitsiou D, Klaic ZB, Prtenjak MT, Moussiopoulos N (2005) The effects of basic flow and topography on the development of the sea breeze over a complex coastal environment. Quart. J. Roy. Meteor. Soc. 131:305–327.

Prandtl L (1952) Essentials of fluid dynamics. Blackie and Son Limited.

Rampanelli G, Zardi D, Rotunno R (2004) Mechanisms of up-valley winds. J. Atmos. Sci. 61:3097–3111.

Rotunno R (1983) On the linear theory of the land and sea breeze. J. Atmos. Sci. 40:1999–2009.

Simpson JE (1996) Diurnal changes in sea-breeze direction. J. of Appl. Meteor. 35:1166–1169.

von Storch H, Zwiers FW (1999) Statistical Analysis in Climate Research. Cambridge University Press.

Whiteman CD (2000) Mountain Meteorology. Oxford University Press.

Wilks DS (1995) Statistical Methods in the Atmospheric Sciences. Academic Press.

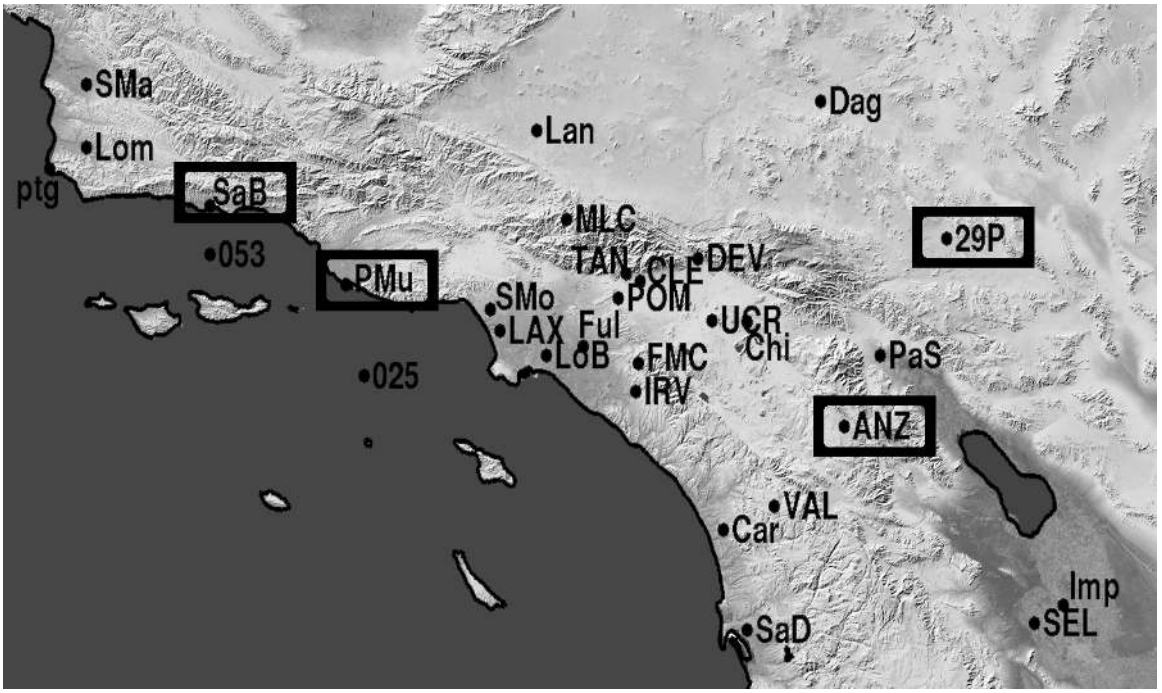

Figure 1: Elevation in Southern California shown in shaded relief. Station identifiers of the 30 stations used in this analysis are shown in black type, with a black period showing actual location. The four boxed stations are used in Fig. 3. This image was generated using the 3 arc second central global shaded relief from the NASA/NGA Shuttle Radar Topography Mission.

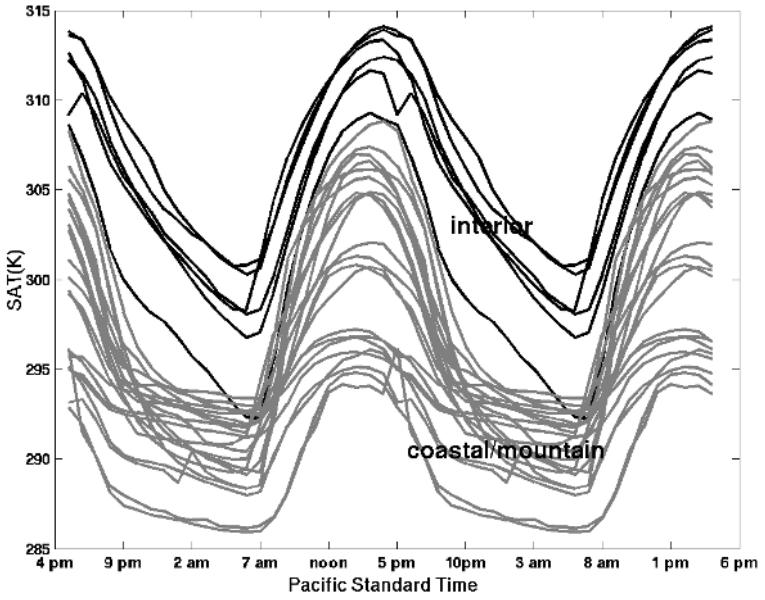

Figure 2: Composite diurnal cycle of SAT in Kelvin at the 27 land observation stations shown in Fig. 1, with hours given in Pacific Standard Time. The buoy stations are not shown because of their small diurnal cycle. Two full diurnal cycles are shown for clarity. Gray lines indicate that the station was on the coastal side of the mountains or within the mountains, and black lines indicate an interior station. The obvious inconsistencies in a few of the composite diurnal cycles are caused by hours in the climatological day with very little data.

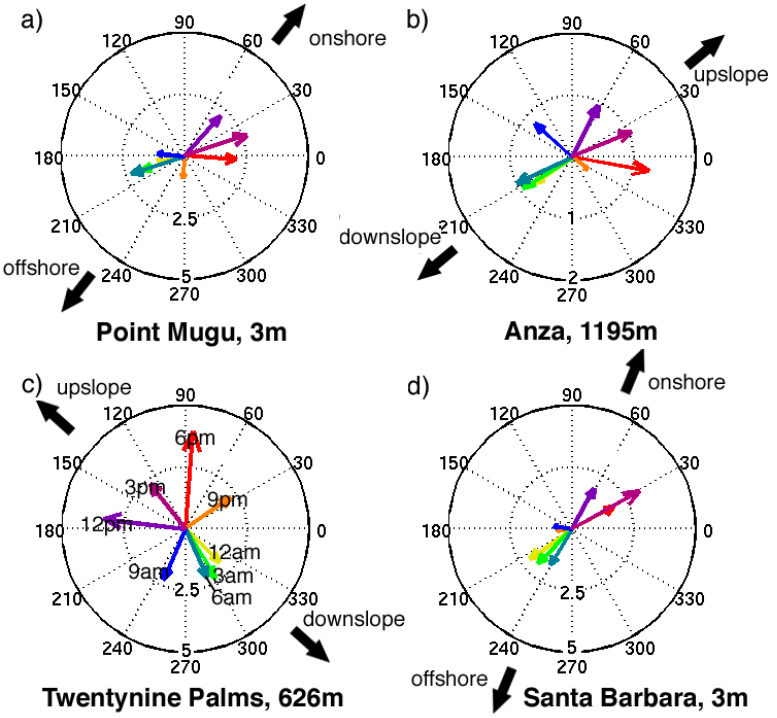

Figure 3: August diurnal near-surface wind variations at the four boxed locations of Fig. 1: a) Point Mugu (b) Anza (c) Twentynine Palms and (d) Santa Barbara. The elevation of each station in meters is given to the right of the station name. The August climatological mean winds were removed prior to plotting to focus on the wind diurnal cycle. The wind anomalies averaged over three hourly values, sampled on the hour, are shown, centered at the following times (with hours in Pacific Standard time): red (6 pm), orange (9 pm), yellow (midnight), green (3 am), aqua (6 am), blue (9 am), violet (noon), and maroon (3 pm). For example, the 6 pm arrow represents an average of the hourly values for 5 pm, 6 pm, and 7 pm. The times corresponding to each color are also shown in (c) at the end of each wind vector. Amplitude is shown in m/s as radial numerals. The black arrows show the direction of greatest topographical gradient for (b) and (c), and show the onshore direction for (a) and (d).

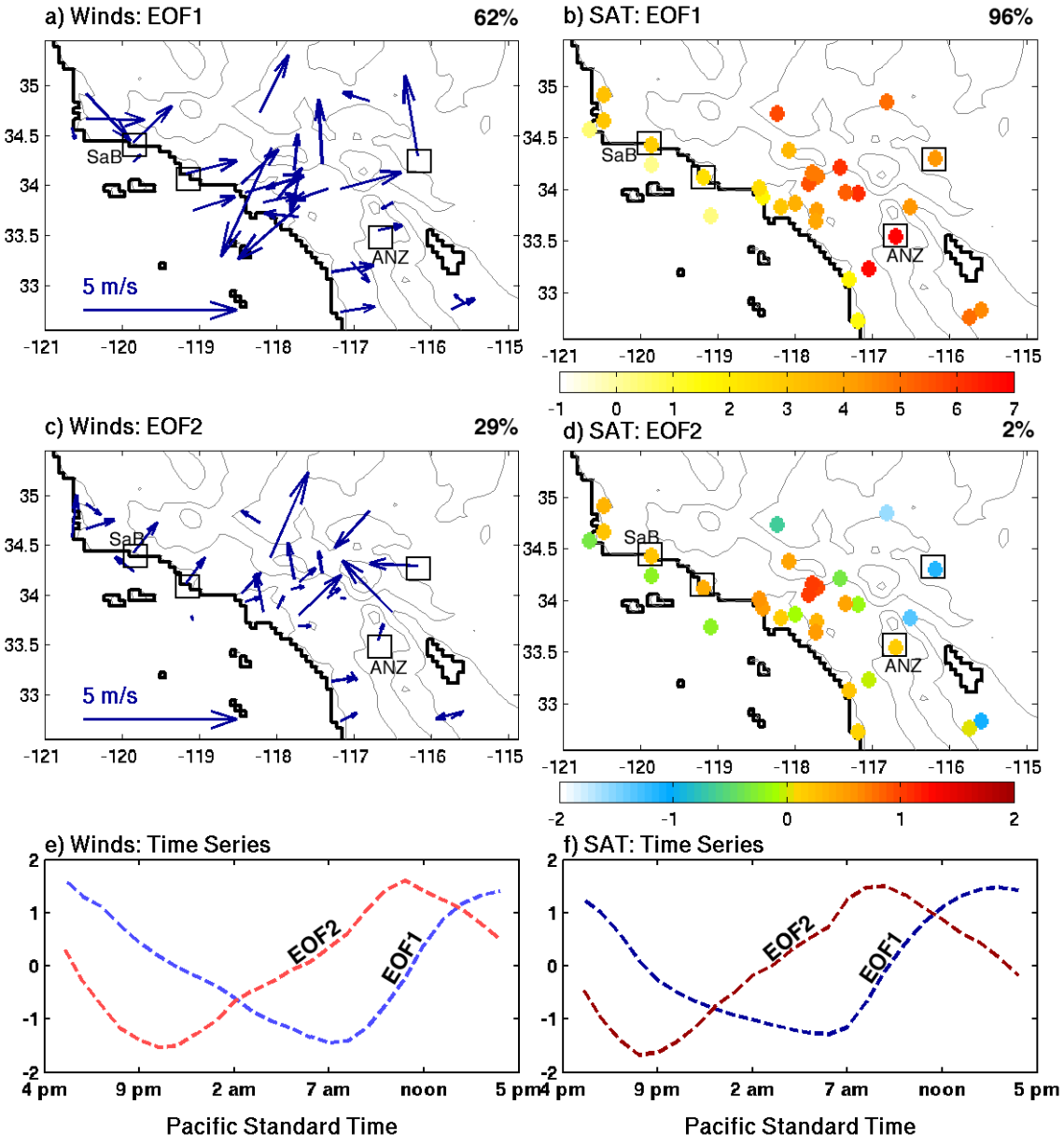

Figure 4: The first two EOFs and associated time series for SAT (b, d, and f) and surface winds (a, c, and e) at the 30 observation stations in Fig. 1, for August composite day anomalies. (a) through (d) show the first two EOFs (spatial displays of the loadings at each location), which account for 62% (96%) and 29%(2%) of the variance for the winds (temperatures). The magnitude of the SAT EOFs (b and d) is indicated by the color of the bullet at each station in K. The four stations chosen for Fig. 3 are boxed in (a) through (d). The associated time series are shown in (e) for wind and (f) for SAT, blue for EOF1 and red for EOF2. Model terrain contours are shown as thin gray lines, every 800m starting at 100m.

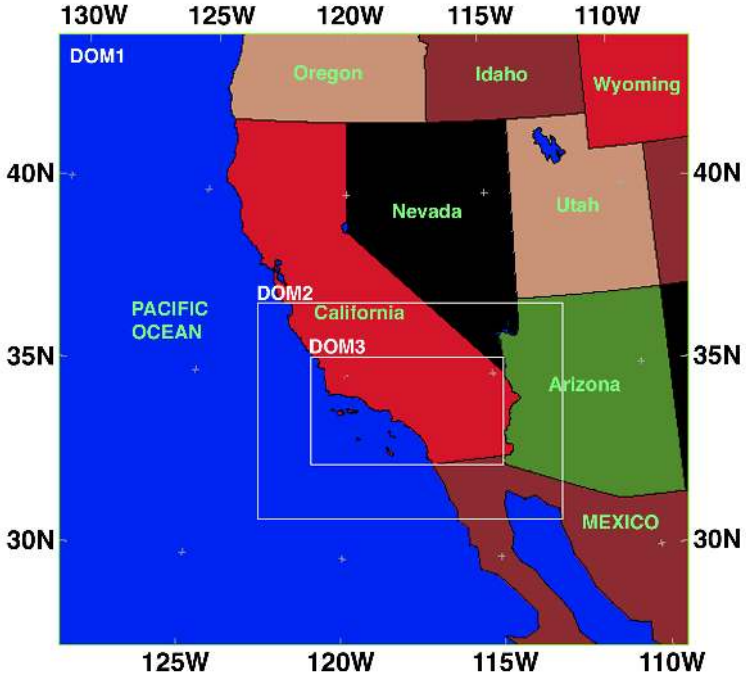

Figure 5: Three domains of the MM5 simulation. The horizontal resolution in the outermost, middle, and innermost domains are 54km, 18km, and 6km, respectively.

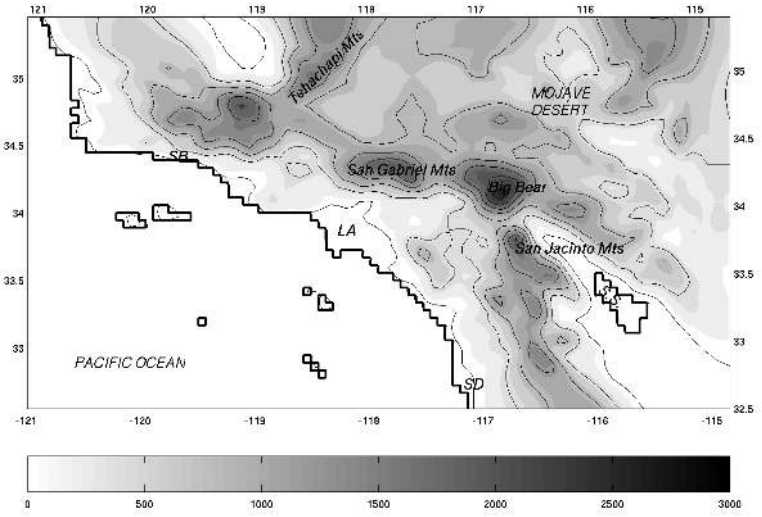

Figure 6: Terrain in the 6km domain of the MM5 simulation. Colorbar shows terrain height in meters, with black terrain contours every 400m starting at 100m. The coastline (shown as the thick black line) illustrates the discretization of the 6km model resolution. Locations referred to in the text are included for orientation, including Los Angeles (LA), Santa Barbara (SB), the Salton Sea (S.S.), and San Diego (SD).

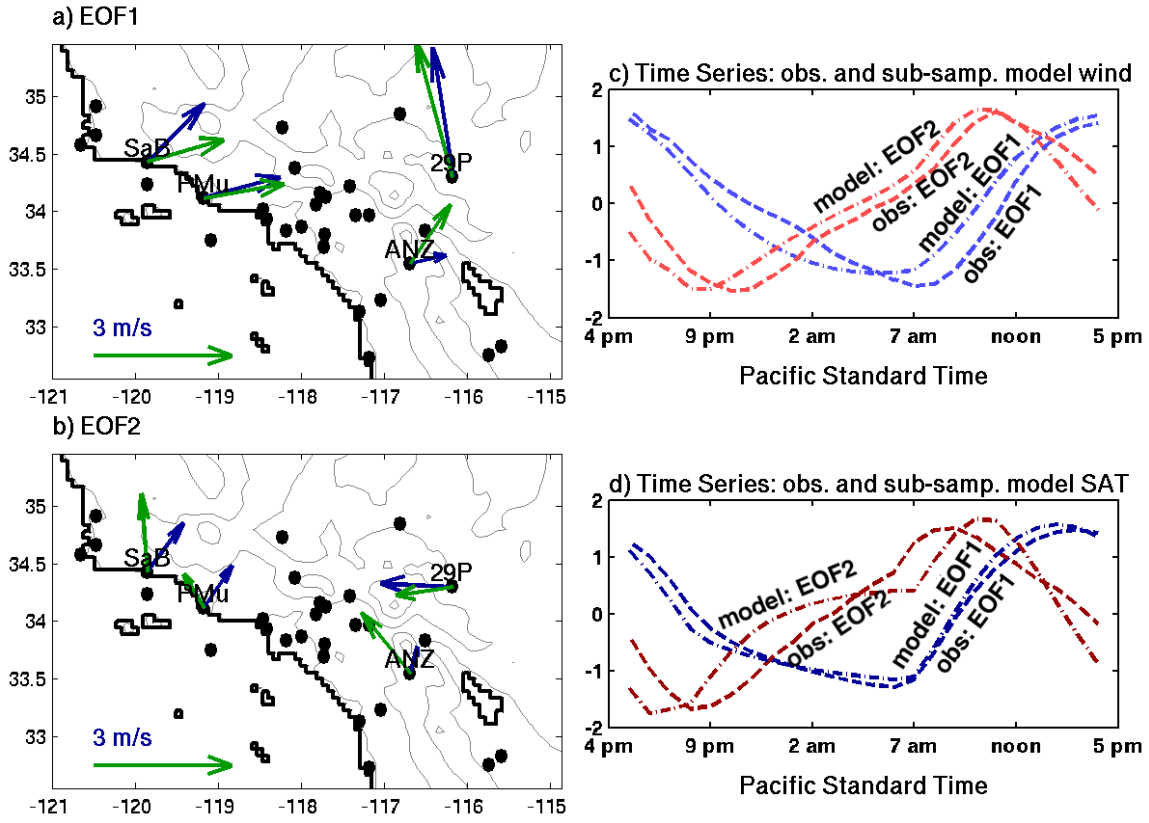

Figure 7: a-c) Spatial displays and associated time series for the EOF analysis of the observed near-surface wind at the 30 stations shown in Fig. 1 (dark blue) and the model generated 10m wind at the 30 closest gridpoints (dark green), for the August composite day. (a) and (b) show the first two EOFs for the station and model winds at the four locations shown in Fig. 3, which account for (a) 71% (62%) and (b) 24% (29%) of the variance for the model (observation) data. Here we juxtapose simulated and observed EOFs only at the four locations from Fig. 3. This is done for clarity of plotting, as these four locations are representative of the degree of model/observation agreement. The associated time series are shown in (c), blue for EOF1 and red for EOF2. The observation time series are the dashed lines, and the sub-sampled model time series are the dot-dashed lines. The black dots are the locations of the other 26 stations used in the EOF analysis. Terrain is shown with gray contours as in Fig. 4. d) Associated time series for the observed SAT EOFs at the 30 stations shown in Fig. 1 (dashed lines) and sub-sampled model generated SAT EOFs at the 30 closest gridpoints (dot-dashed lines), for the August composite day. Variance explained is 96%(97%) and 2%(2%) for the observed (sub-sampled model) EOF1 and EOF2.

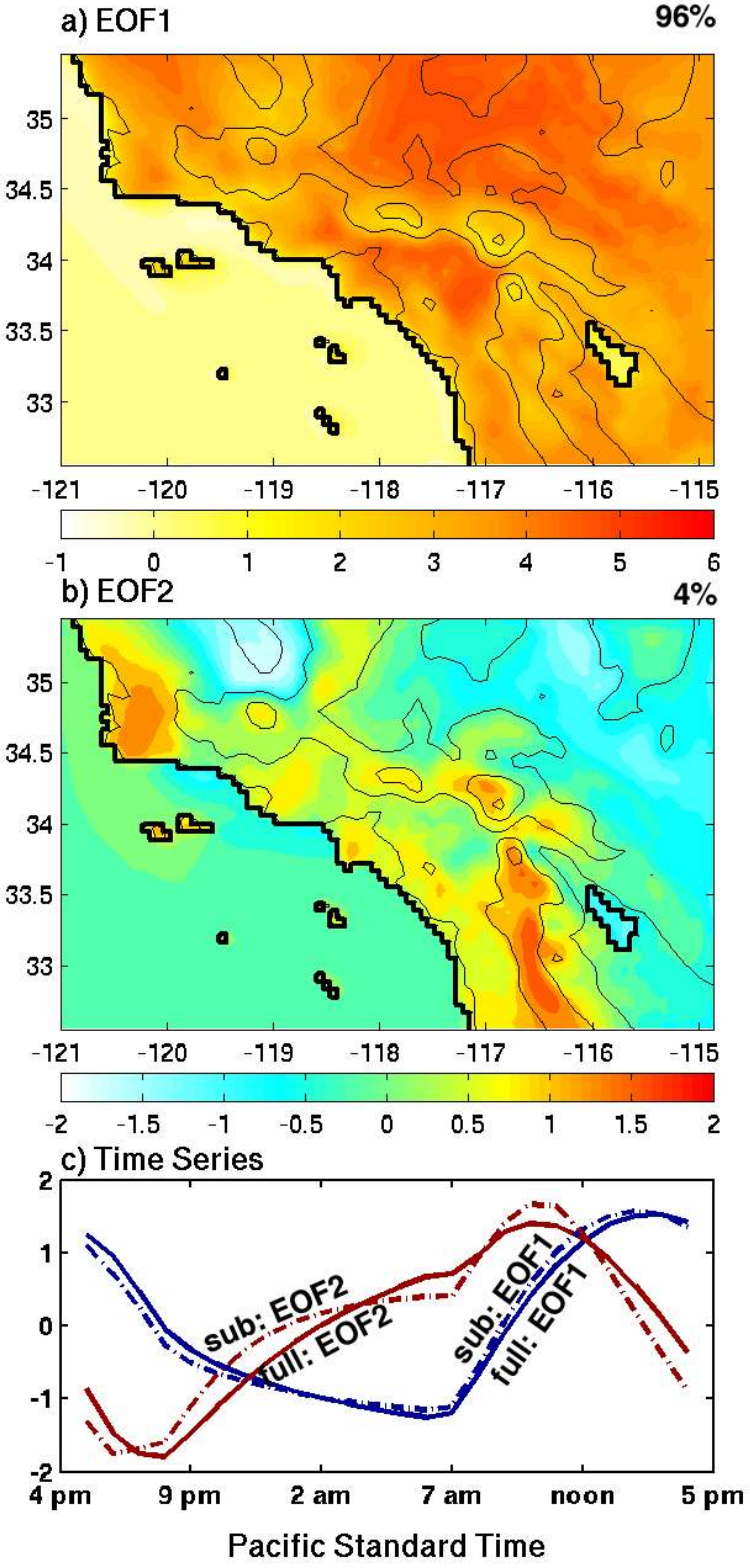

Figure 8: Spatial displays and associated time series for the EOF analysis of the full model generated SAT, for the August composite day. (a) and (b) show the first two EOFs, with colored contours showing loading magnitude in K. The two EOFs account for 96% and 4% of the variance, respectively. The associated principal components are shown in (c), dark blue for EOF1 and dark red for EOF2. For comparison, the time series for the sub-sampled model SAT from Fig. 7d are shown as dot-dashed lines. Terrain is shown with black contours as in Fig. 4.

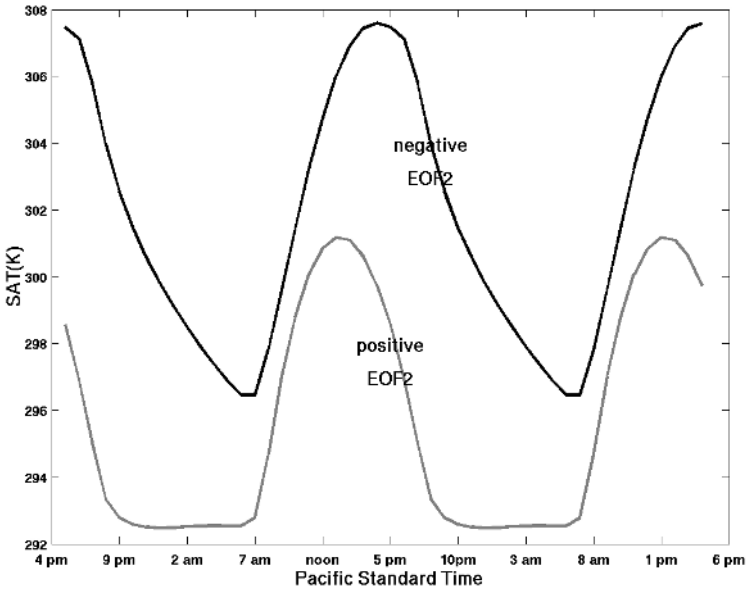

Figure 9: Average diurnal cycle of simulated SAT for gridpoints classified by the value of EOF2 of temperature (Fig. 8b). The gray line is the average diurnal cycle at locations where EOF2 is greater than 1K, which occurs at 238 locations. The black line is the average diurnal cycle where EOF2 is less than -1K, which occurs at 305 locations. The diurnal cycle has been doubled for clarity, and hours are shown in Pacific Standard Time.

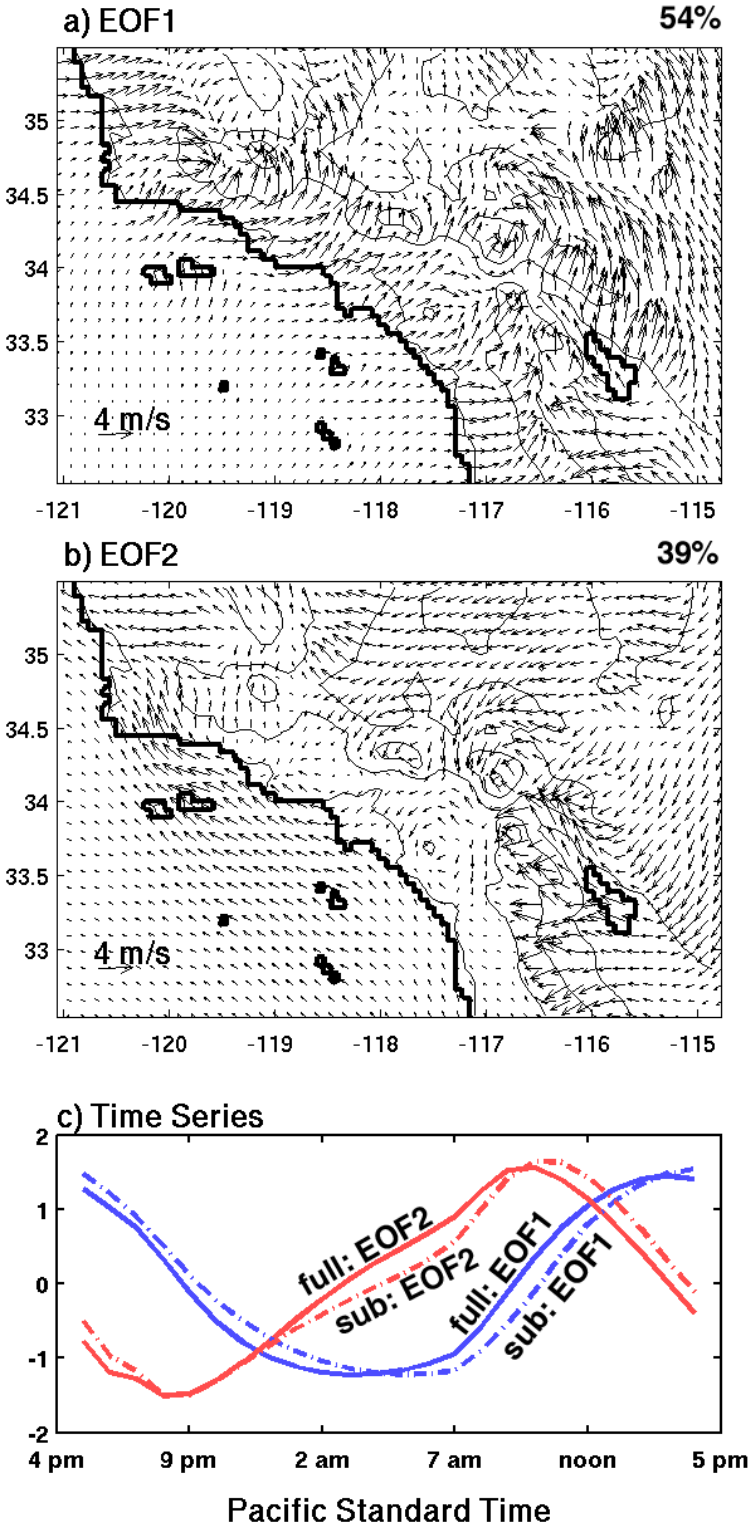

Figure 10: Spatial displays and associated time series for the EOF analysis of the full model generated wind, for the August composite day anomalies. (a) and (b) show the first two EOFs, with arrows to show the wind magnitude and direction. Every other vector in both zonal and meridional directions is suppressed for clarity. The two EOFs account for (a) 54% and (b) 39% of the variance respectively. The associated time series are the solid lines in (c), blue for EOF1 and red for EOF2. For comparison, the time series of the subsampled model winds from Fig. 7c are shown by the dot-dashed lines. Terrain is shown with black contours as in Fig. 4.

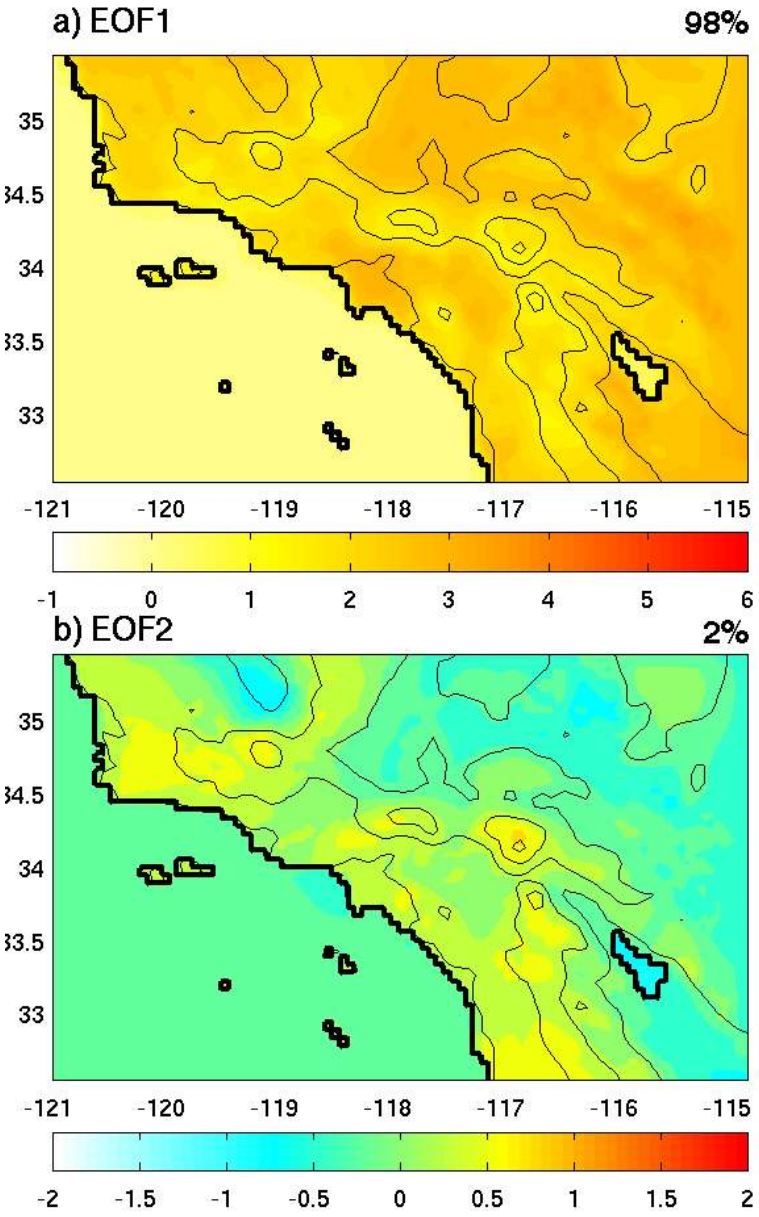

Figure 11: Spatial displays for the EOF analysis of the model generated SAT, for the February composite day anomalies. (a) and (b) show the first two EOFs, with colored contours showing loading magnitude in K. Every other vector in both zonal and meridional directions is suppressed for clarity. The two EOFs account for (a) 98% and (b) 2% of the variance respectively. Terrain is shown with black contours as in Fig. 4.

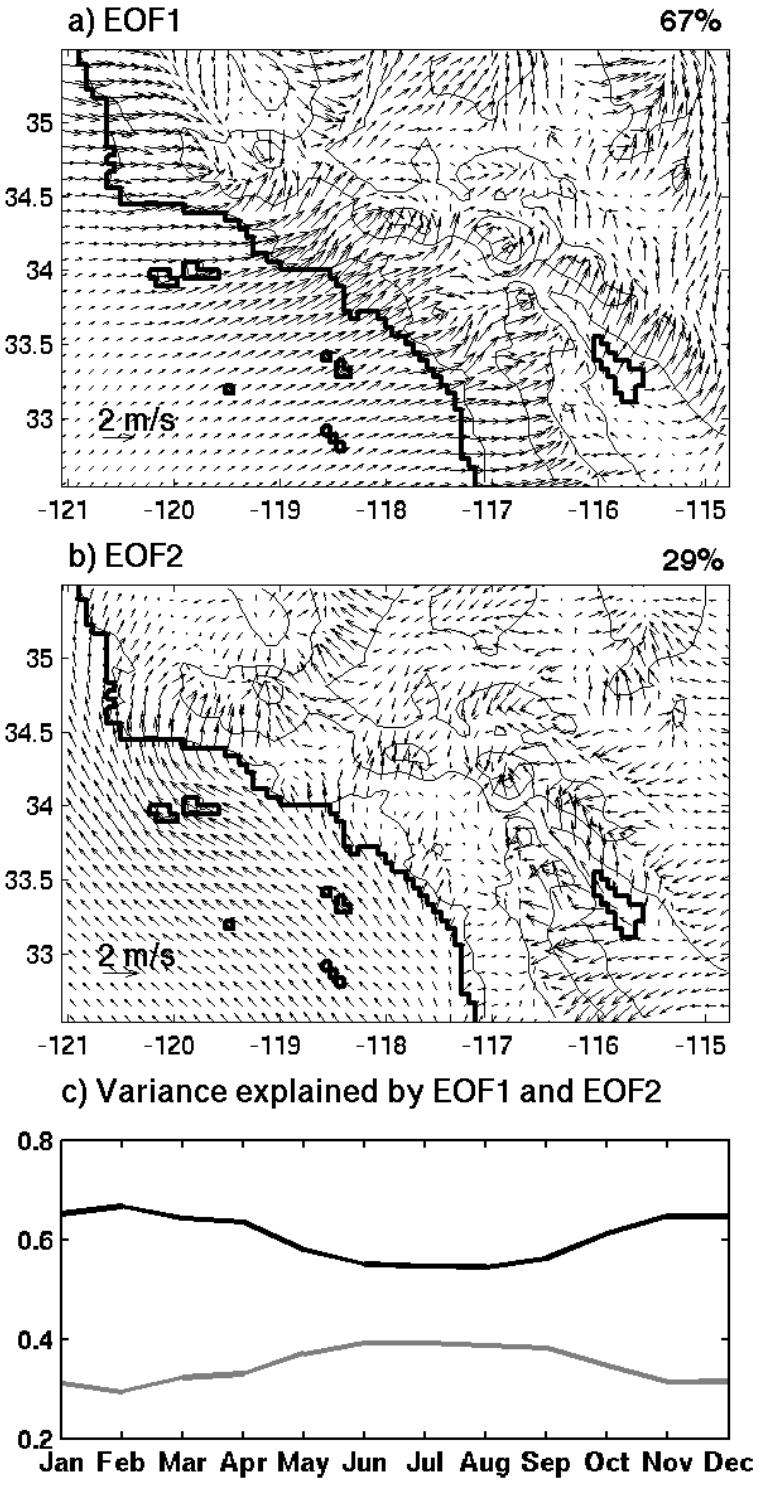

Figure 12: Spatial displays for the EOF analysis of the model generated wind, for the February composite day anomalies, and the variance explained by the two EOFs for each composite month. (a) and (b) show the first two EOFs, with arrows to show the wind magnitude and direction. Every other vector in both zonal and meridional directions is suppressed for clarity. The two EOFs account for (a) 67% and (b) 29% of the variance respectively. Terrain is shown with black contours as in Fig. 4. (c) shows the variance explained by EOF1 (black) and EOF2 (gray) as a function of calendar month.

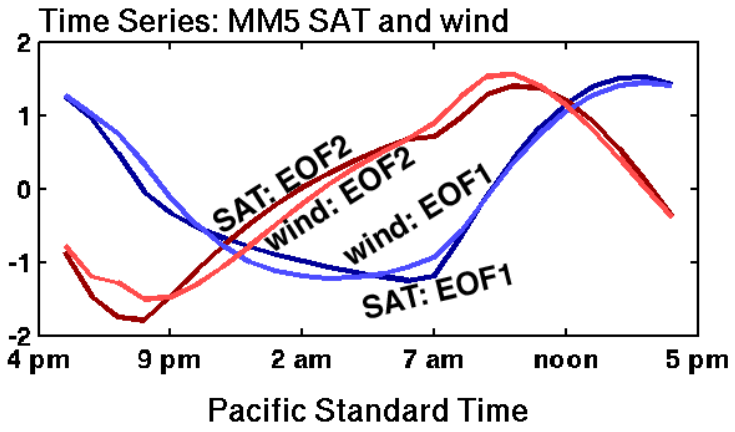

Figure 13: Time series of the model SAT (darker colors) and winds (lighter colors) for August composite day. Variance explained is 96%(54%) and 4%(39%) for the SAT (wind) EOF1 and EOF2.

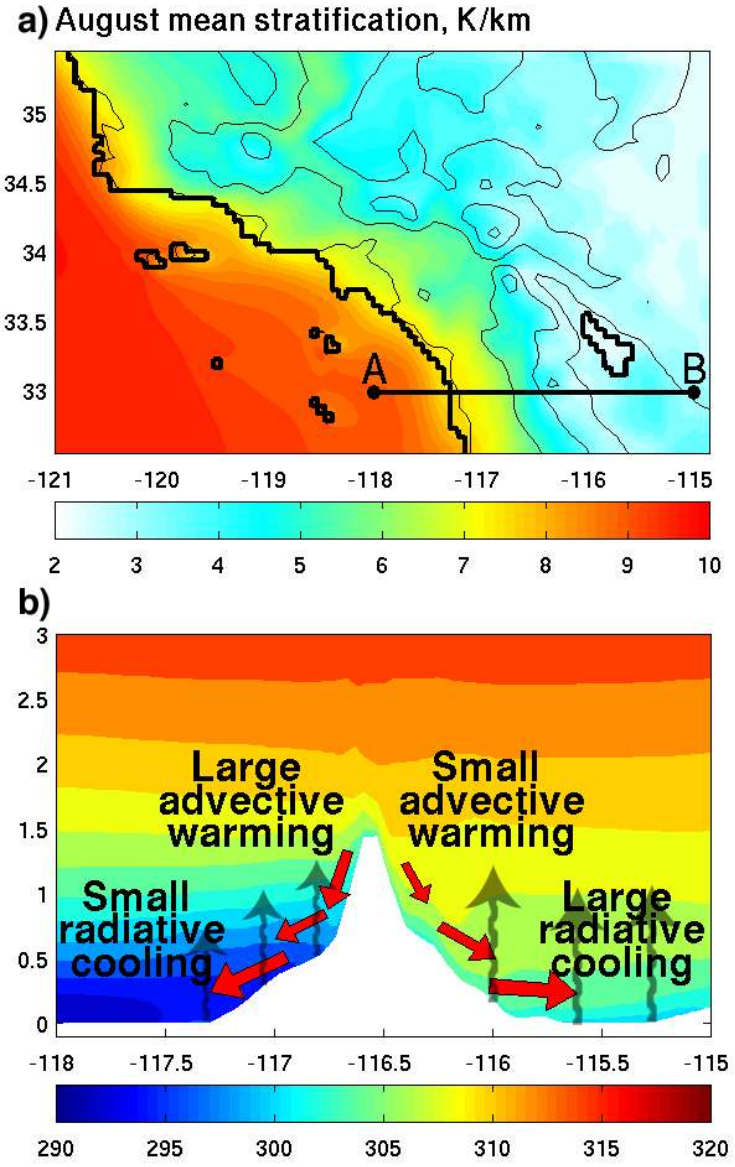

Figure 14: a) Daily average of August composite day stratification of the lower troposphere, in K/km. Here we've calculated stratification using $\frac{\Theta(\sigma=15)-\Theta(\sigma=23)}{z(\sigma=15)-z(\sigma=23)}$, where $\sigma = 15$ denotes the 15th σ level (approximately 700mb or 2.5 km), $\sigma = 23$ denotes the lowest σ level (within 40m of the surface), and Θ is potential temperature. The solid black line that goes from A to B is the location of the cross section shown in (b). b) Longitude-height cross-section at 33N of simulated climatological potential temperature from 9 pm to 1 am (time average) in August. Altitude is shown in km, and Θ in Kelvin. The two dominant processes determining surface air temperature during an August night are indicated schematically. The red arrows represent the advective component of the thermodynamic budget, scaled by the 10 m range-perpendicular wind anomalies for the same time average as the potential temperature, and the gray arrows denote the radiative component, with the arrows scaled to qualitatively convey their relative magnitude.

		$\lvert T.S.1\rvert * \lvert EOF1\rvert$	$\lvert T.S.2\rvert * \lvert EOF2\rvert$	*Monthly mean wind speed*
August	land	4.01	3.61	2.56
	water	1.8	2.5	5.64
February	land	2.65	1.77	1.53
	water	2.7	2.14	2.7

Table 1: Column 1: Area average of the loading magnitude of EOF1 multiplied by the amplitude of its associated time series, in m/s. Column 2: As in column 1, except for EOF2. Column 3: Area average monthly mean wind speed, in m/s. Row 1(2) shows the August (February) climatological values, segregated into land and water points.